

Interdigitated 3-D Silicon Ring Microelectrodes for DEP-Based Particle Manipulation

Xiaoxing Xing, Mengying Zhang, and Levent Yobas, *Member, IEEE*

Abstract—This paper describes the design, the fabrication, and the characterization of an interdigitated 3-D silicon (Si) ring microelectrodes for dielectrophoretic (DEP) manipulation of particles. The 3-D microelectrodes are derived from a high-aspect-ratio comb structure etched in a doped single crystal Si on an insulating dielectric (silicon-on-insulator). Fingers of the comb are evolved into ring microelectrodes once perforated with a linear array of well-defined round lateral constrictions. This is achieved by the segmented finger layout and the Si dry release strategy borrowed from inertial microelectromechanical systems. The fingers and their interspaces are sealed with a cover layer forming a microfluidic flow chamber surrounded by 3-D microelectrodes and accessible via single inlet/outlet. The functionality of the device has been verified on 2- and 10- μm polystyrene microspheres in pressure-driven flow through the ring microelectrodes at 3.3 $\mu\text{L}/\text{min}$ effectively focusing them into streams or trapping them around the fingers at moderate voltage levels (20–40 Vpp). [2012-0209]

Index Terms—Cell, constriction, dielectrophoresis (DEP), electrode, etch, focusing, interdigitated, lateral, manipulation, microelectrode, particle, release, silicon (Si), 3-D.

I. INTRODUCTION

DIELECTROPHORESIS (DEP) has been extensively investigated as an enabling technique for manipulating, separating, and focusing microscopic polarizable particles including cells through a nonuniform electric field [1]. DEP-based manipulation exerts a net force on individual cells based on their distinct dielectric properties [2]. Apart from patterning cells in 3-D microtissue constructs [3], such method of differential dielectric affinity could offer cell isolation and postcapture manipulation without resorting to immuno-based labeling techniques [4], [5]. Using this method, various cell types have been successfully isolated to date including human breast cancer cells and normal blood cells [5]–[8], viable and nonviable yeast cells [9], [10], live and heat-treated listeria cells [11], and plant protoblasts [10]. The cells as they are forced to migrate over a microelectrode array under parabolic velocity profile of hydrodynamic flow experience a net differential force, which eventually affect their rate of elution from micro-

channel [5]. Moreover, the DEP isolation of the cell type of interest has been integrated with gene expression profiling analysis on a chip [12].

Inducing DEP through surface microelectrodes requires fairly low activation voltages that can be directly supplied from a compact waveform generator [13]. Microelectrodes and their configurations are extremely crucial as they define the nonuniform electric-field distribution and the subsequent force field profile manipulating cells. Notable microelectrode configurations are detailed in recent reviews [13]–[15]. These thin-film microelectrodes are relatively simple to fabricate, and yet, their force field quickly wears off away from the surface [10], [16]. Introducing microelectrodes in the flow chamber both on the bottom and on the top surface somewhat addresses the issue [17], nonetheless only if their fields overlap with a precise alignment. Alternatively, microelectrodes can be positioned on the sidewalls in the form of a thin-film metal layer sputtered or evaporated or in the form of a thick-film metal electroplated [18], [19]. Apart from metal, heavily doped single crystal silicon can be structured into sidewall microelectrodes in a flow chamber by deep reactive ion etching (DRIE) [20], [21]. Such 3-D silicon microelectrodes have been shown to exhibit significantly reduced Joule heating effect as compared with the thin-film metal counterparts [22] and a relatively uniform DEP force acting across the channel depth, which is an attractive feature for higher efficiency [23]. All the strategies have been shown to produce effective DEP force on particles but at the expense of the fabrication complexity.

Insulator-based DEP (iDEP) bypasses the issues arising from the microelectrodes [24], [25]. Relying on external wires in contact with the flow chamber, iDEP simplifies the fabrication process considerably. Field lines confined between the insulating boundaries of the flow chamber yield a nonuniform field distribution and a net force that remains effective away from the surface. However, iDEP demands high activation voltages to establish the field intensity across the distanced external electrodes, which requires not only a complex bulky power supply but also extreme care against electric hazard. The difficulty of generating high activation voltages at relatively high frequencies severely restricts the possible use of such technique for a range of applications. More recent techniques, namely, contactless DEP and microcapillary-assisted DEP ($\mu\text{C-DEP}$), also rely on external electrodes yet in contact with liquid electrolyte rather than the sample itself [26]–[28]. These techniques alleviate some of the drawbacks faced in iDEP such as the restrictions on the conductivity of the sample. Both utilize microchannels filled with conductive electrolyte to bring the voltage applied closer to the sample kept apart by a thin

Manuscript received July 19, 2012; revised September 27, 2012; accepted October 2, 2012. Date of publication October 25, 2012; date of current version March 29, 2013. This work was supported by the Research Grant Council of Hong Kong under Grant 621711. Subject Editor G. Stemme.

X. Xing and M. Zhang are with the Department of Electronic and Computer Engineering, The Hong Kong University of Science and Technology, Kowloon, Hong Kong.

L. Yobas is with the Department of Electronic and Computer Engineering and the Division of Biomedical Engineering, The Hong Kong University of Science and Technology, Kowloon, Hong Kong (e-mail: eelyobas@ust.hk).

Color versions of one or more of the figures in this paper are available online at <http://ieeexplore.ieee.org>.

Digital Object Identifier 10.1109/JMEMS.2012.2224641

dielectric partition through which the field must penetrate. The latter further integrates microcapillaries in the partition for enhanced field coupling with minimal fluidic contact warranted by their high fluidic resistance. Still, all these methods, despite their simplistic fabrication gained by leaving out the electrode integration, require relatively high voltages.

Recently, an intriguing design has been proposed in the form of interdigitated coaxial ring microelectrodes for 3-D focusing of cells to replace sheath flow in cytometry [29]. Cells experiencing negative DEP are repelled from the thin-film electrode rings sit on the microchannel boundary and forced into center stream where the field intensity is minimum. The design has been previously implemented by etching microchannels with a curved profile in soda lime glass wafers, patterning on the curved channel profile thin-film gold microelectrodes and then bonding a pair to yield an elliptic channel with ring microelectrodes. Still, this process shares the same concerns regarding the precise wafer-to-wafer alignment and the leak-free bonding.

Here, we introduce a novel microfluidic device, for DEP-based particle manipulation, whereby the interdigitated coaxial ring microelectrodes are monolithically integrated on a single silicon-on-insulator (SOI) wafer through a one-mask process, obviating the need for wafer-to-wafer precision alignment. In the subsequent sections, we detail the design, simulation, and fabrication processes of the device followed by experimental results on the DEP-based separation of 10- and 2- μm microspheres.

II. DESIGN

The device design, as conceptualized in Fig. 1(a), involves a flow chamber confined between a pair of interdigitated Si microelectrodes. Across the flow chamber, individual fingers of the opposing electrodes present a repeating pattern of a 3-D ring constriction with a profile further detailed in Fig. 1(b)–(d). The profile is a result of plasma etching silicon through a mask layout with key features shown in Fig. 1(c). The angles (2α and 2β) define two pointing sharp corners etched into silicon while the distance between them ($2d$) sets the minimum thickness of the silicon partition. The overall etching involves the anisotropic removal of Si interrupted by an isotropic undercutting to pinchoff the partition, forming the ring structure in the region necked by the angles [see Fig. 1(d)].

The ring shape and size can be determined by the geometrical parameters articulated in the mask layout and the dry etching profile controlled by the process conditions, as previously detailed [30]. Earlier, we used the individual constrictions in flow-focusing designs as passive structures for the high-performance generation of emulsions [31]. In contrast, here, the entire structure is made of highly doped silicon situated on a dielectric layer for electrical isolation to act as an electrode.

The layout parameters for all the individual constrictions are assigned as $2\alpha = 135^\circ$, $2\beta = 45^\circ$, and $2d = 20 \mu\text{m}$ for a reasonably large round opening that can pass a stream of particles while exerting an effective DEP force field. Each finger is a cascade of ten of such rings [only three are shown in Fig. 1(a)] for an increased throughput of particles. Moreover, the rings of opposing fingers are self-aligned such that cells

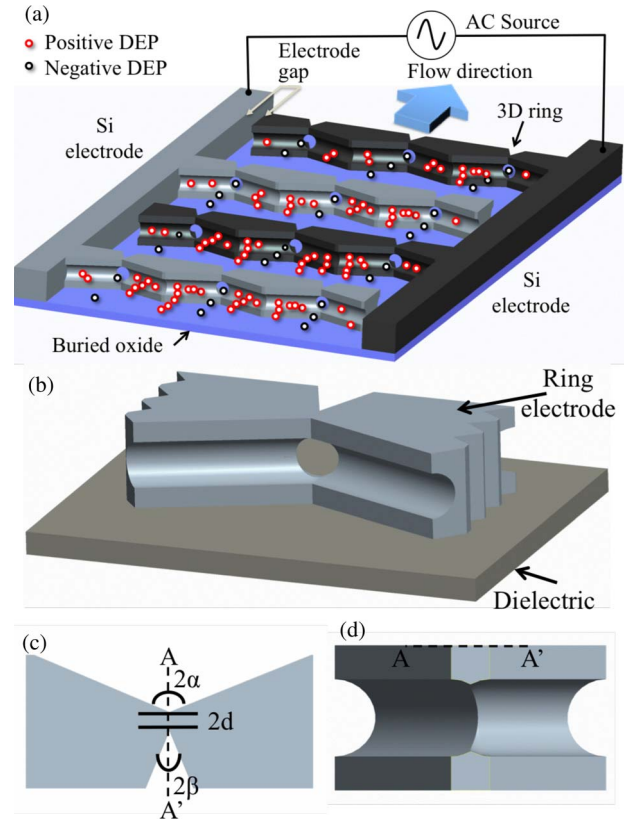


Fig. 1. Conceptual illustrations of the proposed DEP device based on the interdigitated 3-D silicon ring microelectrodes: (a) The overall device with the 3-D microelectrodes monolithically structured on a single SOI wafer without the requirement of wafer-to-wafer alignment. For clarity, the device is shown prior to the capping enclosure. The black and red circles represent two distinct types of particles respond to DEP oppositely while being transported through the device in pressure-driven laminar flow. (b) Oblique view of an individual ring structure etched through the silicon partition underneath the necked region. This single unit repeats across the flow chamber as a fundamental building block in all the microelectrode fingers. (c) Plan view of the necked region shaped by the key design parameters, which also determine, in conjunction with the etching profile, the size and the shape of the ring structure. (d) Cut-away view of the ring structure along the flow direction and perpendicular to AA' plane defined in (c).

or particles driven through them can be focused into parallel streams under negative DEP, as illustrated by the black particles in Fig. 1(a). Meanwhile, those under positive DEP (the red particles) are attracted to the microelectrodes forming pearl chains.

III. THEORY AND SIMULATION

A. DEP Force

The DEP force is exerted on the induced dipole moment of a neutral body in a nonuniform electric field [32]. For a spherical particle (relative permittivity ϵ_p , conductivity σ_p , and radius R) suspended in a medium (relative permittivity ϵ_m and conductivity σ_m) subjected to a nonuniform electric field (angular frequency ω), the time averaged DEP force can be expressed as

$$\bar{F}_{\text{DEP}} = 2\pi\epsilon_m R^3 \text{Re}[K^*(\omega)] \nabla \bar{E}_{\text{rms}}^2 \quad (1)$$

where \bar{E}_{rms} is the root-mean-squared intensity of the electric-field vector, and $K^*(\omega)$ is the complex Clausius–Mossotti (CM)

factor defined in complex permittivities of the particle and the medium is

$$K^*(\omega) = \frac{\varepsilon_p^* - \varepsilon_m^*}{\varepsilon_p^* + 2\varepsilon_m^*} \quad (2)$$

where subscripts p and m refer to the particle and the medium, respectively, and complex permittivity is given by

$$\varepsilon^* = \varepsilon - j\frac{\sigma}{\omega} \quad (3)$$

where j represents $\sqrt{-1}$.

For spherical particles, $\text{Re}[K^*(\omega)]$ typically varies from -0.5 to $+1.0$ according to the relative polarizability of the particles with respect to that of the medium in which they are suspended. A positive value suggests that the particles would get more polarized than the medium and move up the field gradient to the field maxima experiencing positive DEP (pDEP). In contrast, a negative value implies negative DEP (nDEP) with particles moving down the field gradient to the field minima. Switch in the direction occurs at a particular frequency, which is the so-called crossover frequency, at which $\text{Re}[K^*(\omega)]$ is equal to 0 and can be expressed as

$$\omega_C = \frac{1}{2\pi} \sqrt{\frac{(\sigma_m - \sigma_p)(\sigma_p + 2\sigma_m)}{(\varepsilon_m - \varepsilon_p)(\varepsilon_p + 2\varepsilon_m)}}. \quad (4)$$

As shown, the crossover frequency of the particle varies with the conductivity of the medium. For a fixed operating frequency, one might be able to switch the direction of the DEP force by resuspending the particles to a medium of appropriate conductivity, thereby shifting the crossover frequency. In real experiments, however, one rather shifts the operating frequency, for convenience, to control the direction and the magnitude of the DEP force.

The magnitude of the DEP force strongly depends on the electrode design as expressed by $\nabla \bar{E}_{\text{rms}}^2$ in (1). To evaluate $\nabla \bar{E}_{\text{rms}}^2$, a 3-D simulation of the field intensity has been performed in quasi-static ac/dc module of software Comsol 3.5 Multiphysics. The simulated field distribution around a pair of counter microelectrode fingers is shown as aforementioned (three rings per finger) in Fig. 2(a). The field is intensified around the microelectrode edges, in particular, around the convex corners distanced from the rings. On the contrary, the field diminishes within the concave regions around the rings while staying low in the rings [see Fig. 2(b)]. Fig. 2(c) and (d) reveal $\nabla \bar{E}_{\text{rms}}^2$ in line plots as evaluated along the flow direction (dashed line) for practical voltage levels and medium conductivities. As expected, the force exerted on a particle assumes its minimum value when the particle keeps its distance from the either finger (point I). Similarly, the force takes a dip as the particle moves through the ring (point III) but recovers before reaching minimum. The force peaks with the particle approaching (point II) or leaving (point IV) the ring, the latter being slightly more intense due to its proximity to the sharp electrode corners.

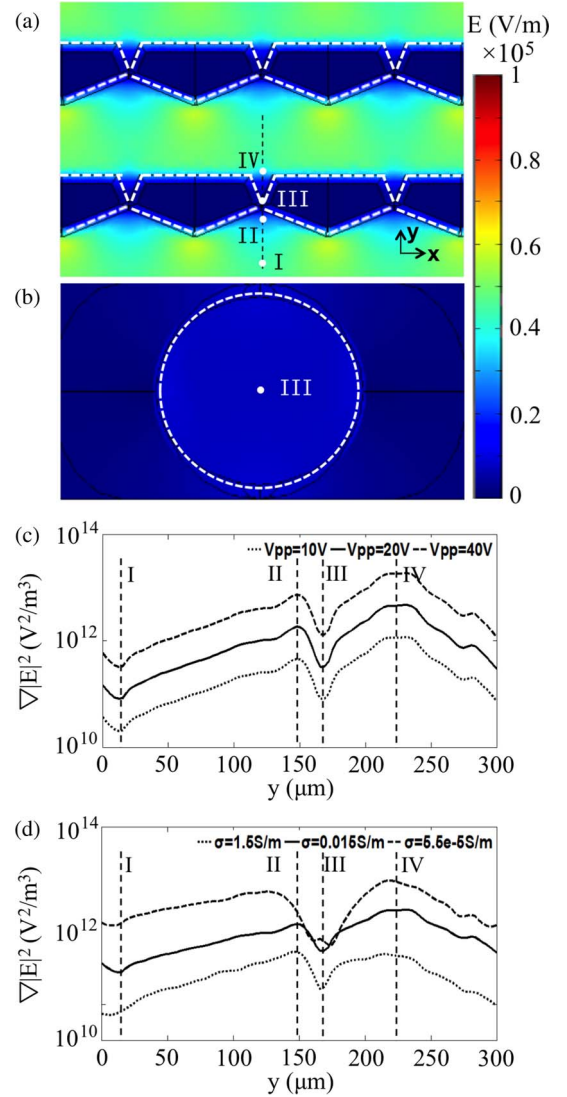


Fig. 2. Results of 3-D numerical simulation across the device. Electric-field intensity at 500 kHz shown for (a) a pair of counter microelectrode fingers (as aforementioned) each represented by three rings and (b) one of the rings. The dashed lines (light color) demarcate (a) the microelectrodes and (b) the ring, while the dark line (a) marks the coordinates along which the gradient of the electric-field intensity squared is displayed in line plots for a set of (c) activation voltages and (d) medium conductivities. Excitation in (a), (b), and (d) is 20 Vpp and 500 kHz.

B. Flow Rate

Particles are transported through pressure-driven flow. Assuming a low Reynolds number (laminar regime) and a parabolic velocity profile, a spherical particle of radius R translating in the device would experience a hydrodynamic (Stokes) drag force according to [33]

$$\bar{F}_{\text{drag}} = 6\pi\eta(\bar{v}_p - \bar{v}_m)R \quad (5)$$

where η is the dynamic viscosity of the medium, and \bar{v}_p and \bar{v}_m are the velocity vectors of the particle and the medium.

In the presence of a nonuniform electric field, the spherical particle translating in the device will reach a terminal velocity when the drag force (5) balances the DEP force (1), i.e.,

$$\bar{v}_p = \bar{v}_m - \mu_{\text{DEP}}\nabla \bar{E}_{\text{rms}}^2 \quad (6)$$

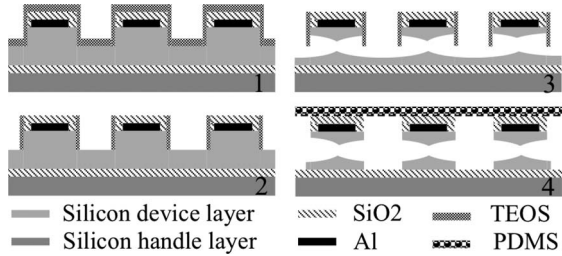


Fig. 3. Description of the fabrication process through SOI cross-sectional schematics after major steps: (1) Deposition of TEOS; (2) removal of TEOS by directional etch; (3) removal of Si by isotropic etch which undercuts the necked region of the Si digits; and (4) removal of TEOS from the sidewalls and Si anisotropic etch to isolate the microelectrodes before a PDMS cover.

where μ_{DEP} is the DEP mobility of the particle, i.e.,

$$\mu_{\text{DEP}} = \frac{\epsilon_m R^2}{3\eta} \text{Re}[K^*(\omega)]. \quad (7)$$

IV. FABRICATION

A. Fabrication

The fabrication of 3-D lateral constrictions (ring structures) is detailed in our earlier work [30]. The process is further developed here to electrically isolate silicon bulk around the constrictions (microelectrodes) by fabricating the entire device on a SOI wafer. Fig. 3 describes the process on SOI schematics in four major steps from a cross-sectional AA' view [see Fig. 1(d)]. These steps will be briefly described here with further details to follow. Step 1 shows three microelectrode fingers partially emerged after being metalized (Al), passivated (SiO₂), and then DRIE. The entire topography is insulated by a layer of tetraethyl orthosilicate (TEOS), which is subsequently cleared off in a directional etch step from trench floors (step 2). The silicon exposed is removed in an isotropic etch step undercutting the necked segments of the fingers defining the ring structures (step 3). After clearing off TEOS from the sidewalls, a second DRIE step is applied to elevate the ring structures further from channel floors (buried-oxide layer) transforming them into constrictions surrounded by electrically isolated bulk silicon. A bonding step encloses the structures with a thin slab of polydimethylsiloxane (PDMS; step 4).

The process used p-type boron-doped (100)-oriented and 100-mm diameter SOI wafer. Resistivity and doping concentration values covered a range of 0.001–0.01 $\Omega \cdot \text{cm}$ and $1 - 10 \times 10^{19} \text{ cm}^{-3}$, respectively. The wafer possessed a 75- μm -thick single crystal silicon device layer on a 2- μm -thick buried oxide. The wafers were cleaned in a piranha solution (H₂SO₄/H₂O₂ 10/1 v/v) for 10 min and then immersed in a solution of diluted HF (HF/H₂O 1/50 v/v) for 60 s, subsequently rinsed in deionized (DI) water and spin-dried in N₂ ambient. For metallization, the wafers were sputtered with Al 4000 Å thick (Varian 3180) and then patterned by dry etching (AST Cirie 200). To register the pattern, a dual-tone photoresist (AZ 5214E) was applied via spin coating (SVG) at 4000 r/min on the sputtered wafers being vapor-primed with an adhesion promoter hexamethyl disylazane (HMDS). After a 2-min soft bake on a 90 °C hot plate, the photoresist was patterned with

TABLE I
DRIE ETCH/PASSIVATION PARAMETERS

PARAMETERS	DRIE I	DRIE II
Platen power (W)	8/–	13/–
Coil power (W)	600/200	600/600
SF ₆ flow rate (sccm)	45/–	160/–
C ₄ F ₈ flow rate (sccm)	15/75	15/100
O ₂ flow rate (sccm)	5/–	18/–
Pressure (mTorr)	17	17
Etch rate ($\mu\text{m}/\text{min}$)	1.25	1.69
Cycle time (s)	7/5.2	13/10

an exposure dose of 29 mW/cm² on a mask aligner (SUSS Microtec MA6). Postexposure bake (PEB) was realized on 110 °C hot plate for 3 min followed by a flood exposure using a dose of 192 mW/cm². The wafers were immersed and agitated in FHD-5 developer for 60 s and then placed on a 120 °C hot plate for 60-s hard bake. This was followed by an oxygen plasma descum to remove organic residues. The exposed Al layer was dry etched (40-sccm BCl₃ and 5-sccm Cl₂ at 25 mTorr, 400-W RF power, and 100-W bias) before stripping off the photoresist layer in an oxygen plasma system (Branson, IPC2000).

The process continued with a plasma-enhanced chemical vapor deposition (STS MESC Multiplex PECVD) for a 1- μm -thick SiO₂ film. The SiO₂ film was then patterned by reactive ion etch (AME 8110 RIE) with CHF₃ plasma (50 mTorr, 74-sccm CHF₃, 6-sccm O₂, and 1200-W coil power). The pattern was registered on a positive resist (HPR 504) repeating the steps of the first lithography with the following modifications. PEB and flood exposure steps were skipped, and an exposure dose of 119 mW/cm² was applied to pattern the resist. An additional hard bake step was performed in a 120 °C oven for about 30 min to release stress, as well as to enhance adhesion of the resist layer. Through the patterned SiO₂ film, the silicon bulk was etched in a DRIE system (STS ICP DRIE). The silicon fingers were partitioned with 40- μm -deep trenches through 160 alternating etch and passivation cycles with process parameters as detailed in Table I (DRIE I). The resist was then stripped off through oxygen plasma.

The 6000-Å-thick TEOS upon deposition was cleared off the trench floor in RIE with CHF₃ plasma (same conditions as aforementioned). With the sidewalls protected by TEOS, the silicon bulk was isotropic etched in SF₆ plasma (130-sccm SF₆, 14-sccm O₂, 94 mTorr, and coil/platen power of 800/11 W). TEOS was then cleared off the sidewalls by dipping the wafer in CH₃COOH : NH₄F : C₂H₆O₂ : H₂O (37:17:17:29 v/v/v) for 30 s with caution to leave sufficient SiO₂ film on the Al layer for proper insulation and as a bonding intermediary. For a complete isolation of the microelectrodes, the remaining silicon was also cleared off the trench floors through a carefully tuned recipe detailed in Table I (DRIE II). Polymer residues deposited on the sidewalls during DRIE were removed by O₂ plasma.

SEM images of various structures after the key process steps are depicted in Fig. 4. Fig. 4(a) shows Si spikes sighted upon the removal of TEOS from the trench floor near a 10- μm -wide isolation trench between the counter electrodes. They were cleared off during Si isotropic etching. Isotropic etching

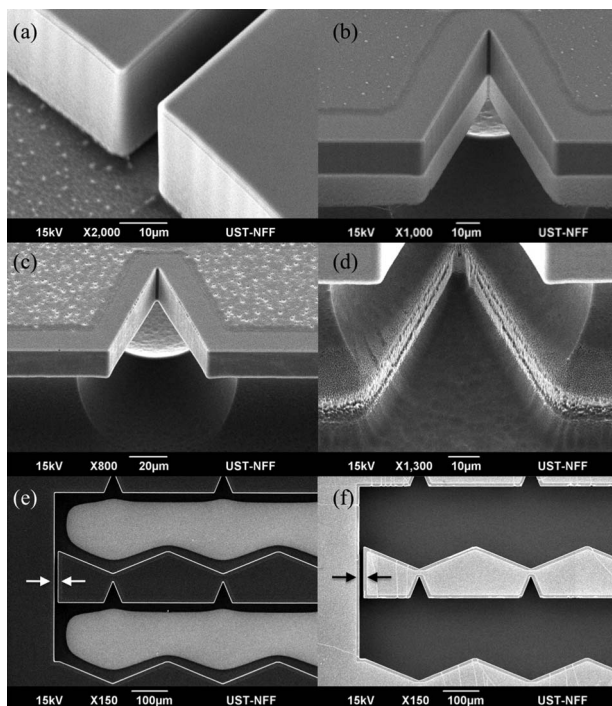


Fig. 4. SEM images featuring various structures after the key process steps: (a) Isolation trench between the opposed electrodes with the trench floor TEOS removed; a ring structure seen (b) behind the overhanging sidewall TEOS and (c) once the sidewall TEOS removed; (d) the second DRIE to elevate and isolate the ring; and the issue (e) encountered with Si removal from (arrows) isolation trenches and (f) addressed by DRIE II listed in Table I.

Si left the sidewall TEOS overhanging in Fig. 4(b), and its removal revealed the ring structure and the etched Si profile in Fig. 4(c). The ring structure was elevated with the second DRIE step during which energetic ions being deflected by the sudden profile change along the sidewall left the rough section observed in Fig. 4(d). This etch step also isolated the counter electrodes by removing Si bulk and exposing the buried-oxide layer underneath. Fig. 4(e) suggests, however, that etching Si completely off the narrow isolation trenches (see arrows) was a challenge that could not be tackled by repeating the etch cycles in DRIE I (see Table I). This was noticed when the etch rate first became extremely slow and then stagnant. Referred to as aspect-ratio-dependent etching (ARDE), this is a well-documented phenomenon in which the etch rate is inversely proportional to trench aspect ratio and then abruptly falls to zero as the etching reaches a critical aspect ratio [34]. The critical aspect ratio for the recipe DRIE I was found to be < 5 , whereas the $10\text{-}\mu\text{m}$ -wide isolation trenches required at least 7.5 to reach $75\text{ }\mu\text{m}$ deep.

ARDE is a mass transport-limited phenomenon largely arising from the depletion of fluorine radicals in the trench bottom and further aggravated by the redeposition of passivation polymer from the upper sidewalls [35]. The higher the aspect ratio for a given trench, the more difficult it gets for reactants to reach the trench bottom, as well as for byproducts to escape. To push the critical aspect ratio further, process adjustments for higher ion energy and more directional ion flux are necessary [36]. The passivation layer at the trench bottom also has to be effectively removed.

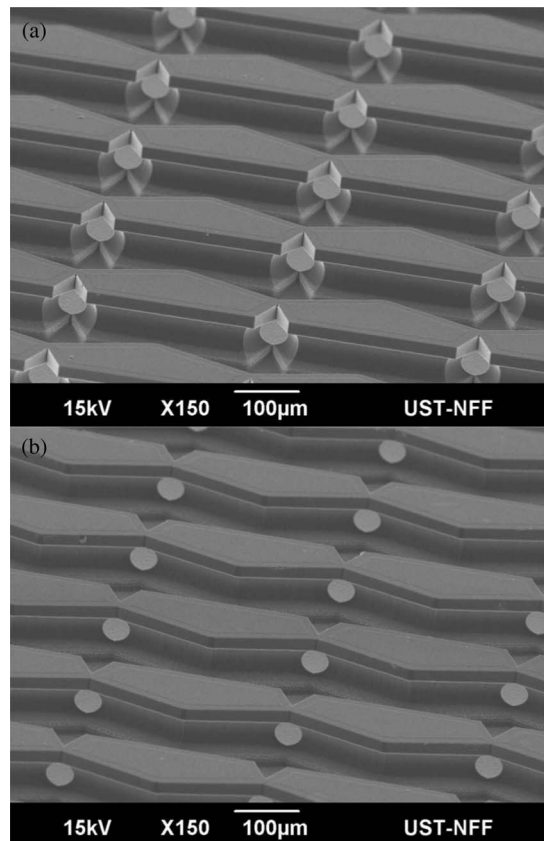


Fig. 5. SEM images of the ring structures from diametrically opposing views: (a) 45° side and (b) 135° side.

Thus, the etch recipe was tuned here as detailed in Table I (DRIE II) such that the relatively high-aspect-ratio isolation trenches receive at the bottom plenty of reactive ion bombardment with increased directivity. First, the cycle interval was almost doubled to give reactants and byproducts enough time to get in and out of the trench bottom. Second, the flow rates of all the gases and primarily of SF_6 were increased to ensure adequate supply of reactants during etching, as well as passivation steps. Third, the platen power was raised to enhance the directivity of ions and warrant an ample ion density at the trench bottom during etching. Fourth, the coil power for the passivation step was also raised for forming a more effective passivation layer against the intensified Si etching to prevent sidewalls from being undercut. Fig. 4(f) proves the effectiveness of the revised process.

Fig. 5 shows a section of a representative device at the conclusion of the process. The SEM images from diametrically opposed views depict the same structure. The rings are highly regular self-aligned underneath the regions necked by 45° and 135° between the pentagon-shaped Si mesa structures. In this particular device, the rings are $35\text{ }\mu\text{m}$ in diameter adequate for small particles and cells to pass through. As shown, the rings are intact with Si bulk $\sim 15\text{ }\mu\text{m}$ thick above and below. Each row of rings defines a single finger of 3-D Si microelectrode and contains a repeat of ten identical units. The fingers fall short of being in contact with the body of the counter microelectrode by a $10\text{-}\mu\text{m}$ narrow gap [see arrow in Fig. 4(e) and (f)].

At the conclusion of the process, the SOI wafer was diced into individual devices. The devices were then bonded with

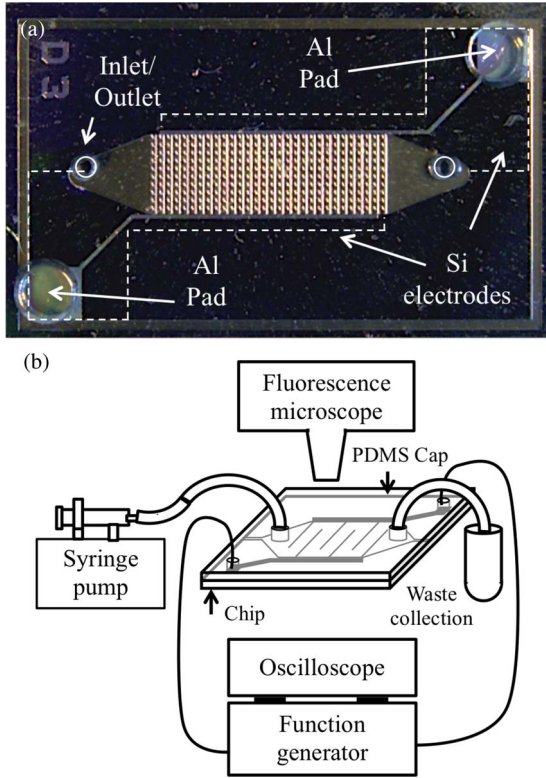


Fig. 6. (a) Picture of a completed device. (b) Schematic of the test setup.

a thin slab of PDMS after activating their surfaces in oxygen plasma (29-W RF for 60 s in Harrick Plasma). Before bonding, fluidic and electrical access ports were punched through the plain PDMS slabs with diameters 1 and 3 mm, respectively.

Fig. 6(a) depicts a representative device obtained. The device measures 22 mm by 10 mm with Si microelectrodes surrounding a flow chamber that is about 15 mm by 5 mm. The microelectrodes form a comb structure extending fingers, 25 pairs in total, into the flow chamber orthogonal to the flow direction. The fingers are 140 μm wide and 160 μm apart maximum. Outside the flow chamber, a pair of trenches 10 μm wide (see dashed lines) isolates the microelectrodes. The Al metal pads on the opposing corners provide electrical access to the microelectrodes through vias bored in the PDMS cover. Electrical contacts to these pads were made by copper wires secured in place with silver paint and epoxy filling.

B. Experimental Setup

The experimental setup is schematically described in Fig. 6(b). A pair of plastic tubes was inserted into the fluidic ports through the PDMS cover. The tube of the inlet port was connected to a 1-mL syringe (BD Tuberculin) controlled by a syringe pump (Harvard Apparatus) to maintain a fixed flow rate. The sample eluted from the outlet tube was collected into a vial. The microelectrodes were activated with a sinusoidal voltage waveform supplied from a function generator (Tektronix CFG 250) and monitored on an oscilloscope (Tektronix TDS 2012C). The device under test was observed through a fluorescence microscope (Nikon ECLIPSE FN1) equipped with a cooled charge-coupled-device camera (SPOT, RT3 Mono). Fluorescent

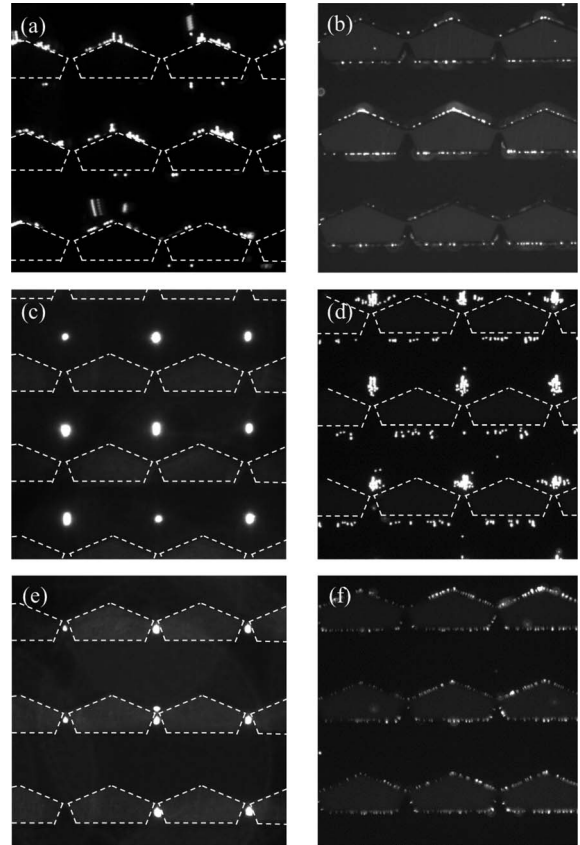


Fig. 7. Fluorescence micrographs of a representative device in which the patterns of microspheres arranged in response to (a) and (b) 1 kHz, (c) and (d) 1 MHz, and (e) and (f) 100 kHz of the voltage excitation: 20 Vpp forming the patterns of 10- μm microspheres in (a), (c), and (e), while 40 Vpp forming the patterns of 2- μm microspheres in (b), (d), and (f). The microspheres in DI water (2×10^{-5} S/m) in the absence of pressure-driven flow exhibit (a) and (b) pDEP, (c) and (d) nDEP, (e) nDEP, and (f) pDEP. The dashed lines demarcate the microelectrodes.

polystyrene microspheres (Bangs Laboratories) were 10 μm (Ex/Em 480/520 nm) and 2 μm (Ex/Em 360/420 nm) in diameter and were resuspended in DI water (5.5×10^{-5} S/m) at the respective concentrations of 5×10^5 and 1.5×10^6 mL^{-1} after a spin/wash at 5000 r/min for 2 min. The ionic conductivities of the solutions were measured by a conductivity meter (Mettler-Toledo, SevenGo Duo pro).

V. MICROFLUIDIC RESULTS

Using the device, the crossover frequency for either size of the microspheres in DI water was independently confirmed in the absence of pressure-driven flow by identifying the frequency of the applied voltage at which the microspheres switched their distinct patterns (see Fig. 7). At 1 kHz, the microspheres concentrate around the electrodes (pDEP). During 1 MHz, they are repelled from the electrodes and accumulate in accordance with nDEP near point I (see Fig. 2). At 100 kHz, however, the patterns are no longer in agreement as 10- μm microspheres still under nDEP move into the rings and 2- μm microspheres under pDEP toward the electrodes. This suggests that the crossover frequencies for 10- and 2- μm microspheres lie on the opposite sides of 100 kHz. They were narrowed down to 3.8 and 300 kHz, respectively.

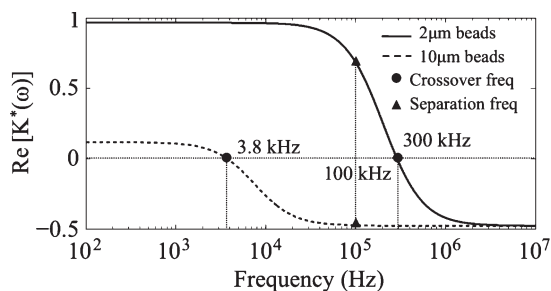


Fig. 8. Frequency plot of the calculated CM factor (real part) for 2- and 10- μm polystyrene microspheres.

Based on these empirical values, the conductivity of the microspheres were derived from (4) and then substituted in (2) to evaluate $\text{Re}[K^*(\omega)]$ over a frequency range, as plotted in Fig. 8. The microspheres were treated according to the homogenous particle model with relative permittivity of 2.5 and particle conductivity given by $\sigma_p = \sigma_{\text{bulk}} + 2K_S/R$, where σ_{bulk} is the polystyrene bulk conductivity, approximately zero, and K_S is the surface conductance of the microspheres, empirically derived as 0.2 and 3.6 nS for 10- and 2- μm microspheres, respectively. These are within the same order of magnitude as those 0.2–2.1 nS obtained from electrorotation of latex particles with a mean diameter of 5–10 μm over a medium conductivity of 2–16 $\mu\text{S}/\text{cm}$ [37]. In the derivation, the permittivity of free space was 8.85×10^{-12} F/m, and the relative permittivity of the DI water was assumed to be 80, while its conductivity is 5.5×10^{-5} S/m as measured.

Having identified the crossover frequencies for the microspheres suspended in DI water, the capability of the device to separate the microspheres of two distinct sizes was subsequently investigated by applying DEP in conjunction with pressure-driven flow. A mixture of microspheres 2 and 10 μm in diameters suspended in DI water was injected into the device at a rate of 3.3 $\mu\text{L}/\text{min}$. Fig. 9 depicts fluorescence micrographs of a section of a device during the experiment. Only one particular size could be seen in either set of images because they were captured through a separate set of filters dedicated to those specific particles. In Fig. 9(a), the 10- μm microspheres were initially shown scattered in the flow but then focused into a narrow stream under nDEP within 3 s upon energizing the microelectrodes through a voltage of 40 Vpp and 100 kHz. This tight focusing occurred as soon as the suspension passed through the first sets of rings. In Fig. 9(b), the 2- μm microspheres, seen scattered even more due to their smaller size, were cleared off the flow under pDEP within about 20 s of the voltage onset. Driven toward the microelectrodes, the 2- μm microspheres were trapped around the silicon structures remained hidden in the rings and the sidewall undercuts in particular.

The microspheres travel through the device with a distinct speed pattern. Fig. 10 describes the characteristic speed in plots showing 10- μm microspheres travelling through a section of the device in successive time-series micrographs. The slope of a fitted line refers to the microsphere speed at that particular instant and depends on the pressure-driven flow rate (1.7 $\mu\text{L}/\text{min}$), the cross-sectional area of the flow, and the DEP field present. Irrespective of the DEP field, the characteristic

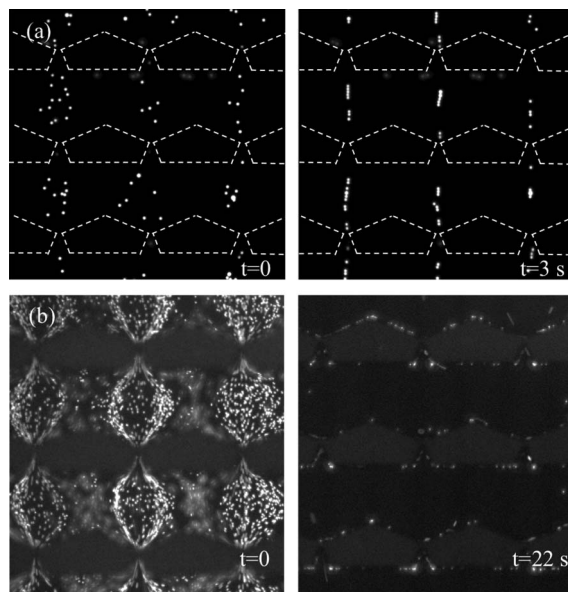


Fig. 9. Fluorescence micrographs of the device undergoing a test with a suspension mixture of 2- and 10- μm microspheres in DI water injected at 3.3 $\mu\text{L}/\text{min}$. A section of the device shown (left) before the voltage onset and (right) after the voltage onset lagged by 3 and 22 s (40 Vpp and 100 kHz). The microspheres shown initially scattered in pressure-driven flow (from top to bottom) yet distinctively responded to DEP: (a) 10- μm microspheres under nDEP remain tightly focused into a narrow stream avoiding (dashed lines) the microelectrodes; (b) 2- μm microspheres under pDEP remain trapped around the microelectrodes with many of them hidden in the rings and the isotropic etched recesses beneath the surface.

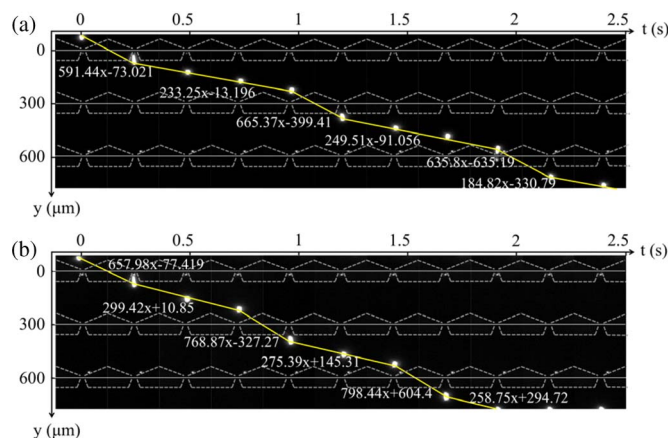


Fig. 10. Plots showing in successive time-series micrographs the distance traveled over time by 10- μm microspheres under pressure-driven flow (1.7 $\mu\text{L}/\text{min}$ from top to bottom) through a section of the device while the field is (a) off and (b) on. Voltage excitation: 20 Vpp and 1 MHz (nDEP). Note the sudden change in speed (the slopes of the fitted lines) as they approach and leave the rings irrespective of the field applied. Also, note the slight gain in speed with the field being on. The dashed lines demarcate the microelectrodes.

speed of the microsphere is such that it shows sudden acceleration and deceleration while approaching and leaving a ring. They travel through a ring faster than through a space between the opposing rings by a factor of about 2.5. This is entirely due to the device geometry as the factor of 2.5 coincides with the ratio of the respective cross-sectional areas sampled by the flow. However, they gain slight momentum, as they experience nDEP at 1 MHz, whether crossing a ring or crossing a space between the rings.

VI. CONCLUSION

An elegant method has been demonstrated for fabricating interdigitated coaxial ring microelectrodes without the cumbersome step of wafer-to-wafer precision alignment and bonding. The method is simple and convenient as it requires only single-mask lithography and subsequent dry etch to structure the ring microelectrodes into single crystal silicon. The 3-D Si microelectrodes define the sidewalls in a microfluidic flow chamber and thus offer a highly effective platform for the DEP-based manipulation of particles as demonstrated here on polystyrene microspheres. The device can find use in various important biological applications such as focusing cells in flow cytometry without the sheath flow [29] and/or enrichment and recovery of circulating rare cells [4], [5] in life science research and in clinical assessment. In those applications, the throughput requirement can be fulfilled by further scaling up the array capacity running multitude of parallel streams through the device [38], [39].

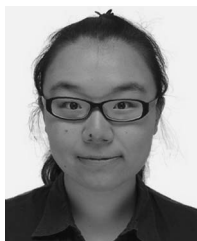
ACKNOWLEDGMENT

The authors would like to thank the staff of the Nanoelectronics Fabrication Facility, The Hong Kong University of Science and Technology, where the reported devices were fabricated. The authors would also like to thank Y. Luo, Z. Cao, and Y. Liu for their help in fabrication and experiments.

REFERENCES

- [1] R. Pethig, "Dielectrophoresis: Status of the theory, technology, and applications," *Biomicrofluidics*, vol. 4, no. 2, pp. 022811-1–022811-35, Jun. 2010.
- [2] Z. R. Gagnon, "Cellular dielectrophoresis: Applications to the characterization, manipulation, separation and patterning of cells," *Electrophoresis*, vol. 32, no. 18, pp. 2466–2487, Sep. 2011.
- [3] D. Choudhury, X. Mo, C. Iliescu, L. L. Tan, W. H. Tong, and H. Yu, "Exploitation of physical and chemical constraints for three-dimensional microtissue construction in microfluidics," *Biomicrofluidics*, vol. 5, no. 2, pp. 022203-1–022203-18, Jun. 2011.
- [4] V. Gupta, I. Jafferji, M. Garza, V. O. Melnikova, D. K. Hasegawa, R. Pethig, and D. W. Davis, "ApoStream, a new dielectrophoretic device for antibody independent isolation and recovery of viable cancer cells from blood," *Biomicrofluidics*, vol. 6, no. 2, pp. 024133-1–024133-14, Jun. 2012.
- [5] P. R. C. Gascoyne and J. V. Vykoukal, "Dielectrophoresis-based sample handling in general-purpose programmable diagnostic instruments," *Proc. IEEE*, vol. 92, no. 1, pp. 22–42, Jan. 2004.
- [6] J. Yang, Y. Huang, X. B. Wang, F. F. Becker, and P. R. C. Gascoyne, "Cell separation on microfabricated electrodes using dielectrophoretic/gravitational field-flow fractionation," *Anal. Chem.*, vol. 71, no. 5, pp. 911–918, Mar. 1999.
- [7] X. B. Wang, J. Yang, Y. Huang, J. Vykoukal, F. F. Becker, and P. R. C. Gascoyne, "Cell separation by dielectrophoretic field-flow fractionation," *Anal. Chem.*, vol. 72, no. 4, pp. 832–839, Feb. 2000.
- [8] F. F. Becker, X.-B. Wang, Y. Huang, R. Pethig, J. V. Vykoukal, and P. R. C. Gascoyne, "Separation of human breast cancer cells from blood by differential dielectric affinity," *Proc. Nat. Acad. Sci. USA*, vol. 92, no. 3, pp. 860–864, Jan. 1995.
- [9] G. H. Markx, M. S. Talary, and R. Pethig, "Separation of viable and non-viable yeast using dielectrophoresis," *J. Biotechnol.*, vol. 32, no. 1, pp. 29–37, Jan. 1994.
- [10] G. H. Markx and R. Pethig, "Dielectrophoretic separation of cells: Continuous separation," *Biotechnol. Bioeng.*, vol. 45, no. 4, pp. 337–343, Feb. 1995.
- [11] H. B. Li and R. Bashir, "Dielectrophoretic separation and manipulation of live and heat-treated cells of *Listeria* on microfabricated devices with interdigitated electrodes," *Sens. Actuators B, Chem.*, vol. 86, no. 2/3, pp. 215–221, Sep. 2002.
- [12] Y. Huang, S. Joo, M. Duhon, M. Heller, B. Wallace, and X. Xu, "Dielectrophoretic cell separation and gene expression profiling on micro-electronic chip arrays," *Anal. Chem.*, vol. 74, no. 14, pp. 3362–3371, Jul. 2002.
- [13] J. Voldman, "Electrical forces for microscale cell manipulation," *Annu. Rev. Biomed. Eng.*, vol. 8, no. 1, pp. 425–454, 2006.
- [14] K. Khoshmanesh, S. Nahavandi, S. Baratchi, A. Mitchell, and K. K. Zadeh, "Dielectrophoretic platforms for bio-microfluidic systems," *Biosens. Bioelectron.*, vol. 26, no. 5, pp. 1800–1814, Jan. 2011.
- [15] B. Cetin and D. Li, "Dielectrophoresis in microfluidics technology," *Electrophoresis*, vol. 32, no. 18, pp. 2410–2427, Sep. 2011.
- [16] J. Voldman, R. A. Braff, M. Toner, M. L. Gray, and M. A. Schimidt, "Holding forces of single-particle dielectrophoretic traps," *Biophys. J.*, vol. 80, no. 1, pp. 531–541, Jan. 2001.
- [17] M. Durr, J. Kentsch, T. Muller, T. Schnelle, and M. Stelzle, "Microdevices for manipulation and accumulation of micro- and nanoparticles by dielectrophoresis," *Electrophoresis*, vol. 24, no. 4, pp. 722–731, Feb. 2003.
- [18] L. Wang, L. Flanagan, and A. P. Lee, "Side-wall vertical electrodes for lateral field microfluidic applications," *J. Microelectromech. Syst.*, vol. 16, no. 2, pp. 454–461, Apr. 2007.
- [19] A. V. Lemoff and A. P. Lee, "An ac magnetohydrodynamic micropump," *Sens. Actuators B, Chem.*, vol. 63, no. 3, pp. 178–185, May 2000.
- [20] C. Iliescu, G. L. Xu, V. Samper, and F. E. H. Tay, "Fabrication of a dielectrophoretic chip with 3D silicon electrodes," *J. Micromech. Microeng.*, vol. 15, no. 3, pp. 494–500, Mar. 2005.
- [21] C. Iliescu, L. Yu, G. Xu, and F. E. H. Tay, "A dielectrophoretic chip with a 3-D electric field gradient," *J. Microelectromech. Syst.*, vol. 15, no. 6, pp. 1506–1513, Dec. 2006.
- [22] F. E. H. Tay, L. M. Yu, A. J. Pang, and C. Iliescu, "Electrical and thermal characterization of a dielectrophoretic chip with 3D electrodes for cell manipulation," *Electrochim. Acta*, vol. 52, no. 8, pp. 2862–2868, Feb. 2007.
- [23] L. M. Yu, C. Iliescu, G. L. Xu, and F. E. H. Tay, "Sequential field-flow cell separation method in a dielectrophoretic chip with 3-D electrodes," *J. Microelectromech. Syst.*, vol. 16, no. 5, pp. 1120–1129, Oct. 2007.
- [24] C.-F. Chou, J. O. Tegenfeldt, O. Bakajin, S. S. Chan, E. C. Cox, N. Darnton, T. Duke, and R. H. Austin, "Electrodeless dielectrophoresis of single and double-stranded DNA," *Biophys. J.*, vol. 83, no. 4, pp. 2170–2179, Oct. 2002.
- [25] B. H. Lapizco-Encinas, B. A. Simmons, E. B. Cummings, and Y. Fintschenko, "Insulator-based dielectrophoresis for the selective concentration and separation of live bacteria in water," *Electrophoresis*, vol. 25, no. 10/11, pp. 1695–1704, Jun. 2004.
- [26] H. Shafiee, J. L. Caldwell, M. B. Sano, and R. V. Davalos, "Contactless dielectrophoresis: A new technique for cell manipulation," *Biomed. Microdevices*, vol. 11, no. 5, pp. 997–1006, Oct. 2009.
- [27] H. Shafiee, M. B. Sano, E. A. Henslee, J. L. Caldwell, and R. V. Davalos, "Selective isolation of live/dead cells using contactless dielectrophoresis (cDEP)," *Lab Chip*, vol. 10, no. 4, pp. 438–445, 2010.
- [28] Y. Luo, X. Cao, P. Huang, and L. Yobas, "Microcapillary-assisted dielectrophoresis (μ C-DEP) for single-particle positionings," *Lab Chip*, vol. 12, no. 20, pp. 4085–4092, Sep. 2012.
- [29] C. Yu, J. Vykoukal, D. M. Vykoukal, J. A. Schwartz, L. Shi, and P. R. C. Gascoyne, "A three-dimensional dielectrophoretic particle focusing channel for microcytometry applications," *J. Microelectromech. Syst.*, vol. 14, no. 3, pp. 480–487, Jun. 2005.
- [30] L. Yobas, R. K. Sharma, R. Nagarajan, V. D. Samper, and P. S. R. Naidu, "Precise profile control of 3D lateral junction traps by 2D mask layout and isotropic etching," *J. Micromech. Microeng.*, vol. 15, no. 2, pp. 386–393, Feb. 2005.
- [31] L. Yobas, S. Martens, W. L. Ong, and N. Ranganathan, "High-performance flow-focusing geometry for spontaneous generation of monodispersed droplets," *Lab Chip*, vol. 6, no. 8, pp. 1073–1079, Jul. 2006.
- [32] H. A. Pohl, *Dielectrophoresis*. Cambridge, U.K.: Cambridge Univ. Press, 1978.
- [33] B. J. Kirby, *Micro- and Nanoscale Fluid Mechanics: Transport in Microfluidic Devices*. New York: Cambridge Univ. Press, 2010.
- [34] B. Wu, A. Kumar, and S. Pamarthy, "High aspect ratio silicon etch: A review," *J. Appl. Phys.*, vol. 108, no. 5, pp. 051101-1–051101-20, Sep. 2010.
- [35] M. A. Blauw, T. Zijlstra, R. A. Bakker, and E. van der Drift, "Kinetics and crystal orientation dependence in high aspect ratio silicon dry etching," *J. Vac. Sci. Technol. B, Microelectron. Nanometer Struct.*, vol. 18, no. 6, pp. 3453–3461, Nov. 2000.
- [36] M. A. Blauw, T. Zijlstra, and E. V. D. Drift, "Balancing the etching and passivation in time-multiplexed deep dry etching of silicon," *J. Vac. Sci. Technol. B, Microelectron. Nanometer Struct.*, vol. 19, no. 6, pp. 2930–2934, Nov. 2001.

- [37] W. M. Arnold, H. P. Schwan, and U. Zimmermann, "Surface conductance and other properties of latex particles measured by electrorotation," *J. Phys. Chem.*, vol. 91, no. 19, pp. 5093–5098, Sep. 1987.
- [38] S. Claire Hur, H. T. Kwong Tse, and D. D. Carlo, "Sheathless inertial cell ordering for extreme throughput flow cytometry," *Lab Chip*, vol. 10, no. 3, pp. 274–280, 2010.
- [39] X. Hu, P. H. Bessette, J. Qian, C. D. Meinhart, P. S. Daugherty, and H. T. Soh, "Marker-specific sorting of rare cells using dielectrophoresis," *Proc. Nat. Acad. Sci. USA*, vol. 102, no. 44, pp. 15 757–15 761, Nov. 2005.



Xiaoxing Xing was born in Hebei, China. She received the B.S. degree in microelectronics from Shanghai Jiao Tong University, Shanghai, China. She is currently working toward the Ph.D. degree in the Department of Electronic and Computer Engineering, The Hong Kong University of Science and Technology, Kowloon, Hong Kong.

Her research interests primarily include silicon-based fabrication, dielectrophoresis, biomicrofluidics, and lab-on-a-chip systems for biomedical applications.



Mengying Zhang received the B.S. degree in applied physics from The University of Science and Technology of China, Chengdu, China, in 2006 and the Ph.D. degree in nanoscience and nanotechnology from The Hong Kong University of Science and Technology (HKUST), Kowloon, Hong Kong, in 2011.

She was a Research Associate with the Department of Electronic and Computer Engineering, HKUST. Her research interests are in microfluidics and droplet-based lab-on-a-chip technologies.



Levent Yobas (M'01) received the B.S. degree in electrical engineering from Hacettepe University, Ankara, Turkey, and the M.S. and Ph.D. degrees both in biomedical engineering from Case Western Reserve University, Cleveland, OH.

He was with the BioMEMS Group, Standard MEMS, Inc., Southbridge and Burlington, MA, developing MEMS for drug screening technologies. From 2002 to 2010, he was with the Institute of Microelectronics, Agency for Science, Technology, and Research (A*STAR), Singapore, where he was a

Senior Research Engineer and then a Member of the Technical Staff in MEMS, BioMEMS, and bioelectronics. He also held adjunct faculty positions with the Bioengineering Division, National University of Singapore, and the School of Electrical and Electronic Engineering, Nanyang Technological University. He is currently with the Department of Electronic and Computer Engineering and the Division of Biomedical Engineering, The Hong Kong University of Science and Technology, Kowloon, Hong Kong. He has mainly published in the areas of nucleic acid analysis, patch clamp electrophysiology, and droplet microfluidics. His earlier work dealt with integrated electrostatic microvalves for a MEMS-based low-cost low-power refreshable Braille display system. His research is mainly focused on silicon-based micro/nanofabrication technologies for life sciences, drug discovery, and point-of-care diagnostics.